PROCEEDINGS A

royalsocietypublishing.org/journal/rspa

Research

Cite this article: Palathingal S, Ananthasuresh GK. 2019 Analytical modelling of spatial deformation pathways in planar and spatial shallow bistable arches. *Proc. R. Soc. A* **475**: 20190164.
http://dx.doi.org/10.1098/rspa.2019.0164

Received: 14 March 2019
Accepted: 24 May 2019

Subject Areas:
structural engineering

Keywords:
snap through, buckling in arches, sway-buckling, lateral-torsional buckling, multi-pathway bistability, eccentric loading

Author for correspondence:
G. K. Ananthasuresh
e-mail: suresh@iisc.ac.in

THE ROYAL SOCIETY
PUBLISHING

Analytical modelling of spatial deformation pathways in planar and spatial shallow bistable arches

Safvan Palathingal and G. K. Ananthasuresh

Department of Mechanical Engineering, Indian Institute of Science, Bengaluru 560012, India

GKA, 0000-0001-6391-7041

We analyse spatial bistable arches and present an analytical model incorporating axial, two transverse bending and torsion energy components. We extend the St. Venant and Michell relationship used in flexural-torsional buckling of planar arches and use it in modelling spatial arches. We study deformation pathways in spatial arches and their effect on critical characteristics of bistability such as back and forth switching forces, and the distance travelled by a point of the arch. We show that not considering spatial deformation leads to incorrect inferences concerning the bistability of planar arches too. Thus, this model serves as a generalized framework for the existing analysis on planar arches since they belong to a subset of spatial arches. Additionally, the effects of eccentric loading on spatial deformations are explored for arches with a range of as-fabricated shapes and boundary conditions, and the results are validated with finite-element analysis.

1. Introduction

Spatial deformation pathways in planar bistable arches reduce switching and switch-back forces. A planar bistable arch can be actuated with an in-plane force so that it remains in its plane throughout as it reaches its other planar stable state. In addition to this planar deformation pathway, the same arch can be actuated to follow a spatial deformation pathway, as shown in figure 1*a*. A comparison between force–displacement characteristics corresponding to spatial and planar deformation pathways is given in figure 1*b*. Our attempt to understand and analytically model spatial deformation pathways in planar bistable arches led us to

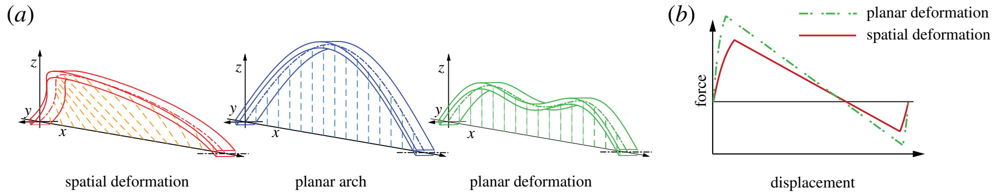

Figure 1. (*a*) Planar and spatial deformation pathways of a planar arch; dashed lines aid visualization of the curvature of the arch during deformation. (*b*) Switching forces of a spatially deforming bistable arch are found to be smaller than those of an arch deforming in the plane. (Online version in colour.)

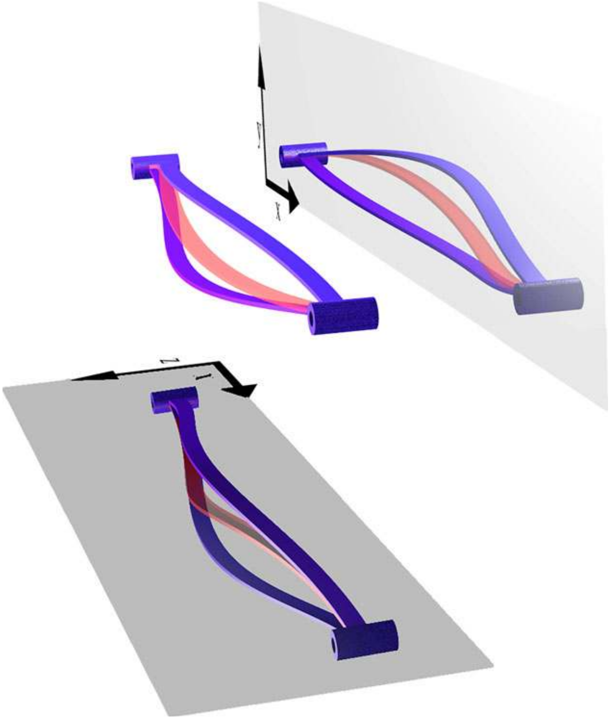

Figure 2. A pinned–pinned spatial arch in its as-fabricated stress-free, in-between stressed and second stressed stable states. (Online version in colour.)

a new and general class of structures, namely spatial bistable arches. As shown in figure 2, curvature of spatial arch is not restricted to a single plane. Two varying orthogonal curvatures of the arch can be seen in the reflections of the arch in xy and xz planes. Spatial arches only exhibit spatial deformation pathways. Spatial arch-profiles of in-between and second stable states of the arch are also given in figure 2. Since planar arches with spatial deformations belong to a subclass of spatial arches, the analytical work presented in this paper captures three-dimensional deformations in both spatial and planar bistable arches.

Although to our knowledge, spatial arches are studied for the first time, flexural-torsional buckling, i.e. spatial deformation in planar arches, is considered before in the literature. Those studies dealt with determining the critical load of buckling, especially in circular arches [1–5]. By contrast, in this work, we consider planar and spatial arches of general profiles to study post-buckling analysis to investigate their bistability.

The literature on bistability is rich with studies on buckled beams [1,6,7], arches [8–10] and shells [11,12]. Bistability in planar shallow arches is well studied for pinned–pinned [8], fixed–fixed [9] and generalized boundary conditions [10]. In planar arches, irrespective of the boundary conditions, bistability arises from the interplay between transverse bending and axial compression strain energies. Bending and compression energies are proportional to squares of change in curvature and arc-length of the arch, respectively. Since there is always a change in curvature associated with a deforming arch, bending energy attains a minimum only in the as-fabricated stress-free state of the arch. On the contrary, change in arch-length can assume minimal values at multiple deformed states of the arch. Existence of two such minimum points in the axial energy landscape is essential to have two minima in the total strain energy curve and thereby is essential for bistability. Intuitively, for arches deforming in planar deformation pathways, minimal-axial-energy points help bistability while bending strain energies at these points hinder bistability. However, when arches deform in spatial deformation pathways, in addition to axial and transverse bending energies, there are torsional and out-of-plane bending energies. We show that the key to modelling these interrelated energy terms is a geometric relation, which we obtain by modifying a St. Venant and Michell relationship discussed in 1969 [13,14].

When an arch deforms spatially, its cross sections undergo displacement in a plane perpendicular to its central axis. Along with the displacement, cross sections rotate about the central axis. The displacement and rotation are related to each other. St. Venant and Michell described this relationship for lateral-torsional buckling analysis in planar arches [13,14]; which we use in this paper for analyzing planar arches with spatial deformation pathways. Furthermore, for the analysis pertaining spatial arches given in figure 2, we generalize the St. Venant and Michell relation considering the additional curvature of the arch. That is to say, when one of curvatures of the arch in the modified relationship is taken to be zero, the relationship reduces to its original form given in [13,14].

First, using the modified St. Venant and Michell relationship, we describe an analytical model that captures spatial deformation in shallow spatial arches that are not stressed in their as-fabricated shape. The model is applicable to arches with varying as-fabricated shapes with fixed–fixed as well as pinned–pinned boundary conditions. Second, we focus on the implications of spatial deformation pathways. We show that these pathways reduce the force required for buckling and post-buckling deformations as compared to planar pathways. In the context of bistability, this is sometimes desirable as it reduces the force required for switching between the equilibrium configurations of the bistable arch. Nonetheless, this also implies that these pathways reduce stiffness and stability of the arch. Thus, geometric and material parameters that excessively favour spatial deformations can adversely affect bistability; we illustrate this with examples. Furthermore, we study the effect of eccentric loading on force–displacement characteristic of spatially deforming arches.

For arches with arbitrary as-fabricated shapes and general boundary conditions, our analytical model improves the understanding of bistability in four ways: (i) analysing spatial bistable arches with reduced switching force; (ii) designing planar arches with reduced switching force owing to spatial bistability; (iii) eliminating the loss of bistability due to spatial deformation pathway in planar bistable arches; (iv) understanding the effect of eccentric loading on switching forces.

2. Analytical model for arches that deform spatially

We present an analytical model for spatial deformations in non-planar arches in the post-buckling regime. Such a model also explains the out-of-plane deformations in planar arches. Let us consider a spatial arch with breadth b, depth t, span L and mid-span height h_{mid} as shown in figure 3. The projections of the central axis of the as-fabricated stress-free shape of the spatial arch in xy and xz planes are denoted as $w_0(x)$ and $u_0(x)$, respectively. The projections of the deformed central line of the spatial arch in xy and xz planes are $w(x)$ and $u(x)$. The initial twist in the cross section is taken

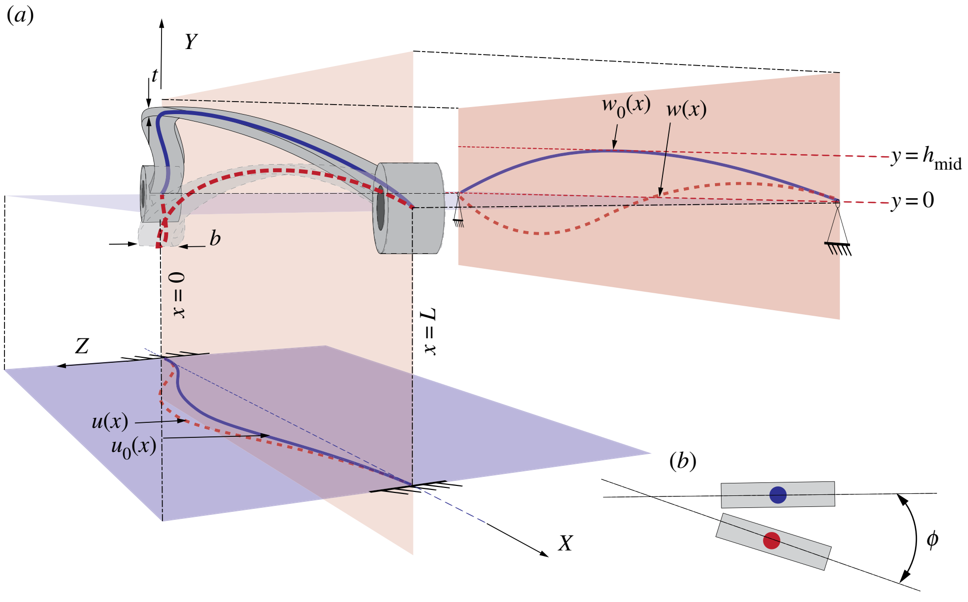

Figure 3. A spatial arch with breadth, b, depth, t, span, L and mid-span height in xy plane, h_{mid}. (Online version in colour.)

to be zero and the rotational displacement of the cross section is denoted by $\phi(x)$. We express these displacements as follows:

$$w_0(x) = h_{\mathrm{mid}} \sum_{i=1}^{\infty} a_i w_i(x), \tag{2.1}$$

$$u_0(x) = h_{\mathrm{mid}} \sum_{i=1}^{\infty} b_i u_i(x), \tag{2.2}$$

$$w(x) = h_{\mathrm{mid}} \sum_{i=1}^{\infty} A_i w_i(x), \tag{2.3}$$

$$u(x) = h_{\mathrm{mid}} \sum_{i=1}^{\infty} B_i u_i(x) \tag{2.4}$$

and

$$\phi(x) = \sum_{i=1}^{\infty} C_i \phi_i(x), \tag{2.5}$$

where w_i, u_i and ϕ_i comprise a basis set that satisfies the boundary conditions of w, u and ϕ, respectively; in fact, they are the buckling mode shapes of a straight column with corresponding boundary conditions. For given a_is and b_is, we determine the mode weights A_is, B_is and C_is of the deformed profile by minimizing the potential energy.

(a) Extension of St. Venant and Michell's relationship

Axial compression, transverse bending, out-of-plane bending and torsional energies are interrelated. We capture this interrelation by extending the St. Venant and Michell's relationship to spatial arches. It is helpful to first understand the relation as presented by St. Venant and Michell for lateral torsional buckling [14] in planar arches. This relation, for an arch in the xy plane with curvature κ_{pxy0} deforming out-of-plane with displacement u_p, and rotation of cross section ϕ_p, the effective change in curvature in xz plane $\Delta\kappa_{pxz}$ is given as follows:

$$\Delta\kappa_{pxz} = \frac{\mathrm{d}^2u_p}{\mathrm{d}x^2} - \phi_p\kappa_{pxy0}. \tag{2.6}$$

Note that the subscript p indicates that these equations are only valid for the planar case. Equation (2.6) implies that the effective change in curvature of projection of the deformed arch-profile, in xz plane, is a combined effect of rotation of cross-section and deformation of the central axis. The first term is the curvature due to the deformation of the arch in the xz plane. Since the coordinates of the deformed central axis of the arch is u_p, the final curvature of the arch is $\mathrm{d}^2u_p/\mathrm{d}x^2$. However, the term $\mathrm{d}^2u_p/\mathrm{d}x^2$ also includes the contribution from projection of curvature of the central axis due to rotation of the cross section. For a positive rotation, ϕ_p, this projection has a positive and upward curvature with a magnitude of $\phi_p\kappa_{pxy0}$, the second term in equation (2.6). Thus, the effective change in curvature is the difference between these two terms. Intuitively, this is equivalent to change in curvature of an arch with an initial curvature $\phi_p\kappa_{pxy0}$ with a deformed profile u_p.

By denoting the curvatures of $w_0(x)$, and $u_0(x)$ as κ_{xy0}, and κ_{xz0}, respectively, the extended St. Venant and Michell's relationship is given by

$$\Delta\kappa_{xz} = \frac{\mathrm{d}^2u}{\mathrm{d}x^2} - (\kappa_{xz0} + \phi\kappa_{xy0}) \tag{2.7}$$

and

$$\Delta\kappa_{xy} = \frac{\mathrm{d}^2w}{\mathrm{d}x^2} - (\kappa_{xy0} - \phi\kappa_{xz0}). \tag{2.8}$$

Equation (2.7) is the equivalent of equation (2.6) for spatial arches. The extra term κ_{xz0} is due to the out-of-plane curvature of the spatial arch. Similarly, equation (2.8) is the change of curvature in the xy plane. However, here the sign of the term $\phi\kappa_{xz0}$ is negative. This is because a positive rotation of cross-section results in a projection of downward curvature in xy plane. Note that ϕ is assumed to be small (i.e. $\sin(\phi) \approx \phi$) in equations (2.7) and (2.8). Furthermore, by taking $\kappa_{xz0} = \mathrm{d}^2u_0/\mathrm{d}x^2$, $\kappa_{xy0} = \mathrm{d}^2w_0/\mathrm{d}x^2$, and ignoring higher-order terms, equations (2.7) and (2.8) are simplified as:

$$\Delta\kappa_{xz} = \frac{\mathrm{d}^2u}{\mathrm{d}x^2} - \left(\kappa_{xz0} + \phi\kappa_{xy0}\right) = \frac{\mathrm{d}^2u}{\mathrm{d}x^2} - \frac{\mathrm{d}^2u_0}{\mathrm{d}x^2} - \phi\frac{\mathrm{d}^2w_0}{\mathrm{d}x^2} \tag{2.9}$$

$$\Delta\kappa_{xy} = \frac{\mathrm{d}^2w}{\mathrm{d}x^2} - \left(\kappa_{xy0} - \phi\kappa_{xz0}\right) = \frac{\mathrm{d}^2w}{\mathrm{d}x^2} - \frac{\mathrm{d}^2w_0}{\mathrm{d}x^2} + \phi\frac{\mathrm{d}^2u_0}{\mathrm{d}x^2}. \tag{2.10}$$

(b) Total potential energy

For an arch with Young's modulus E, and second moment of area for rectangular cross section about z-axis and y-axis, I_z and I_y, the strain energy due to bending is given by

$$\mathrm{SE}_b = \frac{EI_z}{2}\int_0^L (\Delta\kappa_{xy})^2\,\mathrm{d}x + \frac{EI_y}{2}\int_0^L (\Delta\kappa_{xz})^2\,\mathrm{d}x. \tag{2.11}$$

By substituting equations (2.9) and (2.10) into equation (2.11), the bending strain energy becomes

$$\mathrm{SE}_b = \frac{EI_z}{2}\int_0^L \left(\frac{\mathrm{d}^2w}{\mathrm{d}x^2} - \frac{\mathrm{d}^2w_0}{\mathrm{d}x^2} + \phi\frac{\mathrm{d}^2u_0}{\mathrm{d}x^2}\right)^2 \mathrm{d}x + \frac{EI_y}{2}\int_0^L \left(\frac{\mathrm{d}^2u}{\mathrm{d}x^2} - \frac{\mathrm{d}^2u_0}{\mathrm{d}x^2} - \phi\frac{\mathrm{d}^2w_0}{\mathrm{d}x^2}\right)^2 \mathrm{d}x. \tag{2.12}$$

We note in equation (2.12) that the u, w and ϕ contribute to bending strain energy. As the shallow arch deforms, the axial force, f, leads to compression energy, SE_c, which is given by

$$\mathrm{SE}_\mathrm{c} = \tfrac{1}{2}f(s_\mathrm{initial} - s), \tag{2.13}$$

where s is the length of the arch as it deforms and s_initial, the as-fabricated arc-length of the arch. Here, we assume that the axial displacement of the arch is uniform along the length of the arch.

This assumption gives accurate results in planar arches [10] and in spatial arches as we show in subsequent sections. Thus, for a linear elastic material, we write

$$f = Ebt\left(\frac{s_{\text{initial}} - s}{L}\right). \tag{2.14}$$

By assuming the arch to be shallow, i.e. $(\mathrm{d}w_0/\mathrm{d}x)^2 \ll 1$ and $(\mathrm{d}u_0/\mathrm{d}x)^2 \ll 1$, arc-lengths can be approximated as

$$s = \int_0^L \sqrt{1 + \left(\frac{\mathrm{d}w}{\mathrm{d}x}\right)^2 + \left(\frac{\mathrm{d}u}{\mathrm{d}x}\right)^2}\,\mathrm{d}x \approx \int_0^L \left[1 + \frac{1}{2}\left(\frac{\mathrm{d}w}{\mathrm{d}x}\right)^2 + \frac{1}{2}\left(\frac{\mathrm{d}u}{\mathrm{d}x}\right)^2\right]\mathrm{d}x \tag{2.15}$$

and

$$s_{\text{initial}} \approx \int_0^L \left[1 + \frac{1}{2}\left(\frac{\mathrm{d}w_0}{\mathrm{d}x}\right)^2 + \frac{1}{2}\left(\frac{\mathrm{d}u_o}{\mathrm{d}x}\right)^2\right]\mathrm{d}x. \tag{2.16}$$

The rotation of the cross sections, ϕ, results in torsional strain energy given by

$$\mathrm{SE}_t = \frac{GJ}{2}\int_0^L \left(\frac{\mathrm{d}\phi}{\mathrm{d}x}\right)^2 \mathrm{d}x, \tag{2.17}$$

where G is the shear modulus and J is the polar moment of inertia. A point force, F, is applied at the centre of the arch at a point eccentric to the xy plane by e. The displacements of the mid-point along y-axis and z-axis, and the work potential due to these displacements are given by

$$\delta_y = w_0\left(\frac{L}{2}\right) - w\left(\frac{L}{2}\right) + e\phi\left(\frac{L}{2}\right) \tag{2.18}$$

and

$$\mathrm{WP} = -F\delta_y. \tag{2.19}$$

The potential energy, PE, includes bending, compression, and torsional energies, and the work potential. Thus the total potential energy can be expressed as

$$\mathrm{PE} = \mathrm{SE}_b + \mathrm{SE}_c + \mathrm{SE}_t + \mathrm{WP}. \tag{2.20}$$

The equilibrium equations are obtained by minimizing the potential energy with respect to the unknown mode weights, A_is, B_is and C_is as follows:

$$\frac{\mathrm{dPE}}{\mathrm{d}A_i} = 0, \tag{2.21}$$

$$\frac{\mathrm{dPE}}{\mathrm{d}B_i} = 0 \tag{2.22}$$

and

$$\frac{\mathrm{dPE}}{\mathrm{d}C_i} = 0. \tag{2.23}$$

Analytical solutions for equations (2.21)–(2.23) are obtained, as discussed later, for five unknown mode weights. In the subsequent sections, we consider these analytical solutions for varying boundary and loading conditions as well as as-fabricated profiles.

3. Spatial arches

In this section, we analyse spatial arches with pinned–pinned and fixed–fixed boundary conditions and understand the deformation pathways. An example problem is presented for discussing the post-buckling analysis for each of the boundary conditions.

(a) Hinged and fixed support

Consider an arch with pinned–pinned and fixed–fixed boundary conditions in the xy and xz planes, respectively. As mentioned before, the buckling mode shapes of a column with similar boundary conditions are taken as the basis functions to represent the arch-profile as follows:

$$w_i(x) = \sin\left(i\pi\frac{x}{L}\right) \quad i = 1, 2, 3, \ldots \tag{3.1}$$

$$u_j(x) = \begin{cases} 1 - \cos\left(M_j\dfrac{x}{L}\right) & j = 1, 3, 5\ldots \\ 1 - 2\dfrac{x}{L} - \cos\left(M_j\dfrac{x}{L}\right) + 2\dfrac{\sin(M_j(x/L))}{M_j} & j = 2, 4, 6\ldots \end{cases} \tag{3.2}$$

$$M_j = \begin{cases} (j+1)\pi & j = 1, 3, 5\ldots \\ 2.86\pi, 4.92\pi, 6.94\pi\ \ldots & j = 2, 4, 6\ldots \end{cases} \tag{3.3}$$

$$\phi_k(x) = \begin{cases} 1 - \cos\left(M_k\dfrac{x}{L}\right) & k = 1, 3, 5\ldots \\ 1 - 2\dfrac{x}{L} - \cos\left(M_k\dfrac{x}{L}\right) + 2\dfrac{\sin(M_k(x/L))}{M_k} & k = 2, 4, 6\ldots \end{cases} \tag{3.4}$$

and

$$M_k = \begin{cases} (k+1)\pi & k = 1, 3, 5\ldots \\ 2.86\pi, 4.92\pi, 6.94\pi\ \ldots & k = 2, 4, 6\ldots \end{cases} \tag{3.5}$$

Note that M_j and M_k for $j = k = 2, 4, 6, \ldots$ satisfy $\tan(M_j/2) = M_j/2$ [1].

We consider a class of spatial arches with as-fabricated shapes given by

$$w_0(x) = h_{\text{mid}}(a_1 w_1(x) + a_2 w_2(x) + a_3 w_3(x)) \tag{3.6}$$

and

$$u_0(x) = h_{\text{mid}} b_1 u_1(x). \tag{3.7}$$

The mode shapes used for describing the as-fabricated shapes would also be present in the basis set of the deformed profile [15]. Thus, for initial profiles given by equations (3.6) and (3.7), the first three mode shapes are used to approximate the deformations in the xy plane and one mode shape to approximate the deformed profile in the xz plane as follows:

$$w(x) = h_{\text{mid}}\left(A_1 w_1(x) + A_2 w_2(x) + A_3 w_3(x)\right), \tag{3.8}$$

$$u(x) = h_{\text{mid}} B_1 u_1(x) \tag{3.9}$$

and

$$\phi(x) = C_1 \phi_1(x). \tag{3.10}$$

Note that with this choice of basis functions, we have six unknowns, for which analytical solutions are obtained. The applied load is resisted by the stiffness of the arch, which results in the arch having an undulating curvature in the loading plane. Hence, we assume a larger number of mode shapes to express the deformed arch-profile in the loading plane compared to the plane perpendicular to it, where, undulations are absent. Therefore, in this case, we use three mode shapes to capture the in-plane deformation and one mode shape each for both out-of-plane deformation as well as rotation.

To obtain the F-δ_y characteristics we solve for six unknowns namely, A_1, A_2, A_3, B_1, C_1 and F using five equilibrium equations obtained by minimizing the total potential energy with respect to each of the unknown mode weights (i.e. equations (2.21)–(2.23)) and equation (2.18).

By substituting, equations (3.6)–(3.10) in equation (2.20), the equilibrium equations can be expressed as:

$$\frac{\mathrm{dPE}}{\mathrm{d}A_1} = Fh_{\mathrm{mid}} - \frac{Ebh_{\mathrm{mid}}^2 t^3\pi^3(64C_1/b_15 + \pi a_1 - \pi A_1)}{24L^3} + \frac{A_1Ebh_{\mathrm{mid}}^4 t\pi^4({A_1}^2 + 4{A_2}^2 + 9{A_3}^2 + 4{B_1}^2 - {a_1}^2 - 4{a_2}^2 - 9{a_3}^2 - 4{b_1}^2)}{8L^3} = 0, \quad (3.11)$$

$$\frac{\mathrm{dPE}}{\mathrm{d}A_2} = \frac{2Ebh_{\mathrm{mid}}^2 t^3\pi^4(A_2 - a_2)}{3L^3} + \frac{A_2Ebh_{\mathrm{mid}}^4 t\pi^4({A_1}^2 + 4{A_2}^2 + 9{A_3}^2 + 4{B_1}^2 - {a_1}^2 - 4{a_2}^2 - 9{a_3}^2 - 4{b_1}^2)}{2L^3} = 0, \quad (3.12)$$

$$\frac{\mathrm{dPE}}{\mathrm{d}A_3} = \frac{Ebh_{\mathrm{mid}}^2 t^3\pi^3(3264C_1b_1/35 - 81\pi a_3 + 81\pi A_3)}{24L^3} - Fh_{\mathrm{mid}} + \frac{9A_3Ebh_{\mathrm{mid}}^4 t\pi^4({A_1}^2 + 4{A_2}^2 + 9{A_3}^2 + 4{B_1}^2 - {a_1}^2 - 4{a_2}^2 - 9{a_3}^2 - 4{b_1}^2)}{8L^3} = 0, \quad (3.13)$$

$$\frac{\mathrm{dPE}}{\mathrm{d}B_1} = \frac{Eb^3h_{\mathrm{mid}}^2 t\pi^3(64C_1a_1/5 - 3264C_1a_3/35 - 16\pi b_1 + 16\pi B_1)}{24L^3} + \frac{B_1Ebh_{\mathrm{mid}}^4 t\pi^4({A_1}^2 + 4{A_2}^2 + 9{A_3}^2 + 4{B_1}^2 - {a_1}^2 - 4{a_2}^2 - 9{a_3}^2 - 4{b_1}^2)}{2L^3} = 0 \quad (3.14)$$

and

$$\frac{\mathrm{dPE}}{\mathrm{d}C_1} = \frac{2C_1GJ\pi^2}{L} + 2Fe + \frac{Ebb_1h_{\mathrm{mid}}^2 t^3\pi^3(816A_3 - 112A_1 + 112a_1 - 816a_3 + 245\pi C_1b_1)}{210L^3} \times \frac{Eb^3h_{\mathrm{mid}}^2 t\pi^3}{24L^3}\left(\frac{64B_1a_1}{5} - \frac{3264B_1a_3}{35} - \frac{64a_1b_1}{5} + \frac{3264a_3b_1}{35} + \frac{5\pi C_1{a_1}^2}{2} + 20\pi C_1{a_2}^2\right) + \frac{Eb^3h_{\mathrm{mid}}^2 t\pi^3}{24L^3}\left(\frac{243\pi C_1{a_3}^2}{2} - \frac{45\pi C_1a_1a_3}{2}\right) = 0. \quad (3.15)$$

The expressions for respective energy terms leading to equations (3.11)–(3.15) are given in appendix A. To understand the nature of deformations, let us take the as-fabricated shape to constitute only the fundamental buckling mode shape, i.e. only the first mode shape, in both the planes of the arch. So, we substitute $a_1 = 1$, $b_1 = 0.5$, $h_{\mathrm{mid}} = 5\,\mathrm{mm}$, $b = 2\,\mathrm{mm}$, $t = 0.5\,\mathrm{mm}$, $L = 100\,\mathrm{mm}$, and the remaining a_is and e are taken to be zero in equations (2.18) and (3.11)–(3.15). E and ν of the material are taken as 2.1 GPa and 0.3, respectively. We solve for F using equations (3.11)–(3.15), for δ_y ranging from 0 mm to twice the height of the arch, i.e. 10 mm. The force–displacement characteristics obtained after ignoring complex solutions are shown in figure 4*a*.

In the figure 4*a*, points O and T refer to the first and second stable states of the arch, respectively. Corresponding to each combination of paths between O and T, there are multiple deformation pathways that the arch can take to switch between these stable states. Note that on pathways OABCFHIT, OABDEFHIT and OABDGHIT arch switches symmetrically, i.e. with $A_2 = 0$. And it switches asymmetrically along OACEGIT.

It is not straightforward to predict the preferred deformation pathway from F-δ_y curves in figure 4*a*. We infer this by visualizing the potential energy landscape of the arch given in figure 4*c*. Each curve in the landscape corresponds to the potential energy curve along δ_y for a constant force. The extremum of the curve is the equilibrium position of the arch for the assumed force value. Hence, when there are multiple pathways having the same force value for a given displacement, there will be as many extrema for that displacement. Thus, by generating potential energy curves for the force values in the F-δ_y curve, each deformation pathway can be compared by observing the locations of extrema across these curves. The solid curves (cyan) passing through point O in figure 4*c* correspond to force–displacement curve OABDGH. And the solid curves

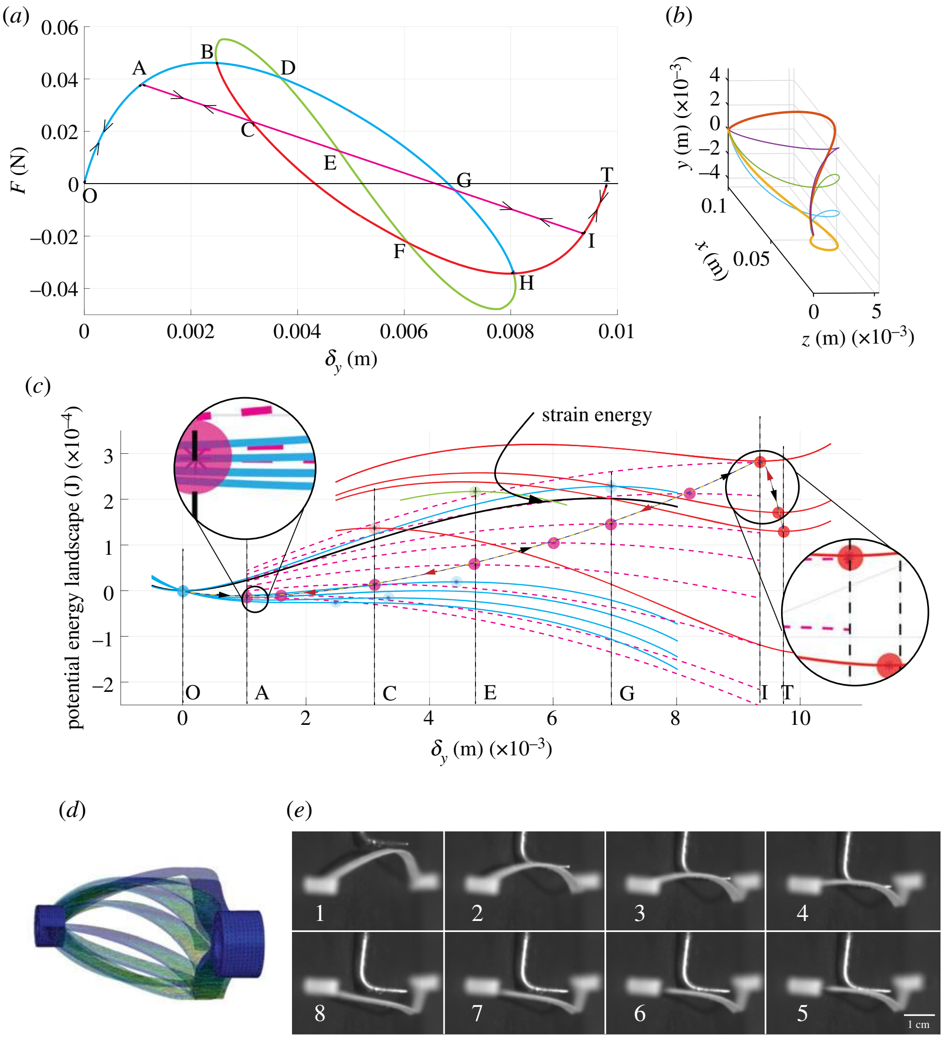

Figure 4. (*a*) Force–displacement characteristics, (*b*) asymmetric deformation pathway, (*c*) potential energy landscape for OACEGIT pathway, (*d*) deformation pathway from ABAQUS and (*e*) time-lapse using high-speed photography (a hook that pushed the arch can be seen in the figures) for a spatial bistable arch with pinned–pinned boundary conditions. (Online version in colour.)

(red) passing through displacement at point T follows the force pathway TIHFCB. The dashed curves (magenta) are for the force values along ACEGI and short green curve passing through E corresponds to BDEFH pathway.

The points of extrema on the curves in figure 4*c* are annotated with a circular marker. It is helpful to visualize the marker to be a ball on the hill or valley formed by the potential energy curve. When the arch is in the stable equilibrium state at O, the force is zero; so, the ball is resting on the black solid curve (labelled as the strain energy) at O. The ball rolls along the minima on cyan curves from point O to point A. Since there are two pathways for the force value at point A, the ball has the option to either continue rolling on extrema of solid curves or to jump to the maxima on the dashed curve. In figure 4*c*, we observe that dashed potential energy curve at A (enlarged view is shown in the inset) is positioned below the solid curve. Thus, the ball rolls from the minimum on the solid curve to maxima on the dashed curve. It continues on the dashed curve until I, where the asymmetric solution cease to exist. Note that the solution pathway does not change at the points C, E and G since the potential energy of the respective intersecting

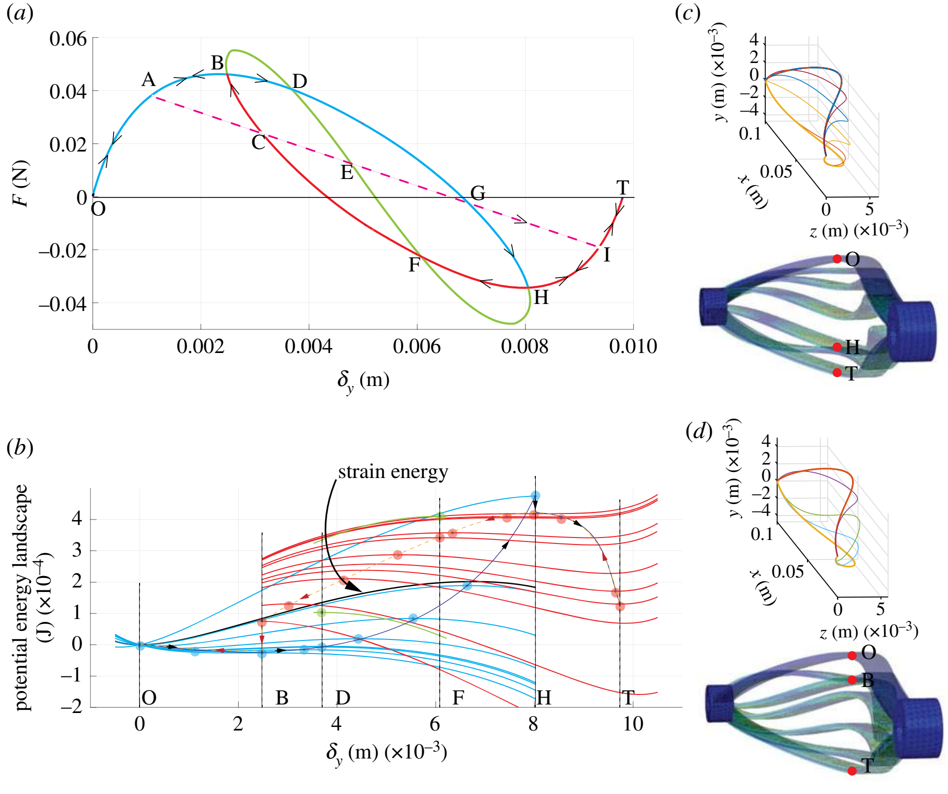

Figure 5. (*a*) Force–displacement characteristics, (*b*) potential energy landscape, (*c*) time-lapses of switching and (*d*) switch-back for symmetric deformation pathways of a pinned–pinned spatial bistable arch. (Online version in colour.)

pathways are larger than the asymmetric deformation pathway ACEGI at these points. Hence, the pathway that arch takes is OACEGIT. That is to say that the arch deforms symmetrically (OA and IT) near its stable states and asymmetrically (ACEGI) in between, as shown in figure 4*b*. The predicted deformation pathway from the model is reproduced using finite-element analysis (FEA) software ABAQUS [16], in figure 4*d*. See appendix B for a quantitative validation using FEA. Furthermore, a 3D-printed prototype switching in asymmetrically along OACEGIT is depicted in figure 4*e* using high-speed photography. The prototype is made using Verowhite, a material used in an Objet260 Connex 3D-printer. The deformed configurations were captured using a high-speed camera, Photron SA5, at the speed of 2000 frames per second.

Now, if we consider the switch-back deformation of the arch, similar arguments are valid as the arch retraces the path while switching back and follows TIGECAO. However, this is not always the case; bistable arches can switch and switch-back along two different pathways. Let us consider a case where the asymmetric mode of switching is constrained, i.e. the arch cannot deform along the pathway ACEGI anymore. Hence, the arch can only take the deformation pathways shown in figure 5*a*. Let us observe the implications of this restriction in the potential energy landscape given in figure 5*b*. The ball starts from point O on the solid cyan curve and continues to deform along the curve OABDGH since the extrema on BCFHIT pathway is at a higher potential energy at B. The pathway does not change at point D too since the potential energy corresponding to BDEFH is at a larger value. At point H, it switches to the pathway BCFHIT and achieves the second stable state along the curve HIT. While switching back, the arch retraces the switching curve till point H since there is no other pathway the arch can assume until this point. At point H, since the pathway HGDBAO is at a higher potential energy, the ball continues to roll along TIHFCB. At point B, it returns to BAO and reaches the initial stress-free at point O. Again, note that the pathway does not change due to HFEDB at point F. Thus, the pathway for switching and switch-back are OABDGHIT and TIHFCBAO, respectively. Time lapses of arch switching and switching-back from the model and ABAQUS are given in figure 4*c*,*d*, respectively. The FEA simulation in ABAQUS is carried out with a symmetric constraint with respect to a plane parallel to the yz plane passing through the mid-span of the arch. A physical intuition for the lack of smoothness in the force–displacement characteristics at point H while switching and at point B while switching back is evident in these time lapses. At these points, the curvature of the arch snaps symmetrically and flips its curvature—a sudden movement—resulting in sharp points on the F-δ_y curve. In the next subsection, we consider spatial bistable arches with fixed–fixed boundary conditions. For the sake of brevity, we restrict our discussion to the force–displacement characteristics and resulting deformation pathways without examining their potential energy landscape.

(b) fixed–fixed support

For a spatial arch with fixed supports, deformations in both xy and xz planes have fixed–fixed boundary conditions. Hence, similar to the case of pinned–pinned arch, u_j and ϕ_k are taken as equations (3.2) and (3.4), respectively, and w_i as:

$$w_i(x) = \begin{cases} 1 - \cos\left(M_i \dfrac{x}{L}\right) & i = 1, 3, 5 \ldots \\ 1 - 2\dfrac{x}{L} - \cos\left(M_i \dfrac{x}{L}\right) + 2\dfrac{\sin(M_i(x/L))}{M_i} & i = 2, 4, 6 \ldots \end{cases} \tag{3.16}$$

and

$$M_i = \begin{cases} (i+1)\pi & i = 1, 3, 5 \ldots \\ 2.86\pi, 4.92\pi, 6.94\pi \ldots & i = 2, 4, 6 \ldots \end{cases} \tag{3.17}$$

We consider fixed arches with first harmonics in their as-fabricated shapes given by:

$$w_0(x) = h_{\text{mid}}\left(a_1 w_1(x) + a_2 w_2(x) + a_3 w_3(x)\right), \tag{3.18}$$

$$u_0(x) = h_{\text{mid}} b_1 u_1(x), \tag{3.19}$$

$$w(x) = h_{\text{mid}}\left(A_1 w_1(x) + A_2 w_2(x) + A_3 w_3(x)\right), \tag{3.20}$$

$$u(x) = h_{\text{mid}} B_1 u_1(x) \tag{3.21}$$

and

$$\phi(x) = C_1 \phi_1(x) \tag{3.22}$$

The equilibrium equations obtained by minimizing the potential energy equation (2.20) and simplifying using equations (3.18)–(3.22) can be written as follows:

$$\begin{aligned} \frac{\mathrm{dPE}}{\mathrm{d}A_1} = 2Fh_{\text{mid}} &- \frac{2Ebh_{\text{mid}}^2 t^3 \pi^4 (a_1 - A_1 + C_1 b_1)}{3L^3} + \frac{2A_1 Ebh_{\text{mid}}^4 t\pi^2}{L^2} \frac{({B_1}^2 - {b_1}^2)\pi^2}{L} \\ &+ \frac{A_1 Ebh_{\text{mid}}^4 t\pi^2}{L^2}\left(\frac{2\pi^2 {A_1}^2 - 4{A_2}^2 + 8\pi^2 {A_3}^2}{L} - \frac{{A_2}^2 {M_2}^2 (\cos(M_2) + 3)}{2L(\cos(M_2) - 1)}\right) \\ &- \frac{A_1 Ebh_{\text{mid}}^4 t\pi^2}{L^2}\left(\frac{2\pi^2 {a_1}^2 - 4{a_2}^2 + 8\pi^2 {a_3}^2}{L} - \frac{{M_2}^2 {a_2}^2 (\cos(M_2) + 3)}{2L(\cos(M_2) - 1)}\right) = 0, \end{aligned} \tag{3.23}$$

$$\begin{aligned} \frac{\mathrm{dPE}}{\mathrm{d}A_2} = \frac{E{M_2}^4 bh_{\text{mid}}^2 t^3 (A_2 - a_2)}{24L^3} - \\ \frac{A_2 Ebh_{\text{mid}}^4 t(8\cos(M_2) + 3{M_2}^2 + {M_2}^2\cos(M_2) - 8)}{4L^2(\cos(M_2) - 1)}\left(\frac{2\pi^2 {a_1}^2 - 4{a_2}^2 + 8\pi^2 {a_3}^2}{L}\right) \end{aligned}$$

$$
\begin{aligned}
&+\frac{A_2Ebh_{\mathrm{mid}}^4t(8\cos(M_2)+3{M_2}^2+{M_2}^2\cos(M_2)-8)}{4L^2(\cos(M_2)-1)}\left(\frac{{M_2}^2{a_2}^2(\cos(M_2)+3)}{2L(\cos(M_2)-1)}\right)\\
&-\frac{A_2Ebh_{\mathrm{mid}}^4t(8\cos(M_2)+3{M_2}^2+{M_2}^2\cos(M_2)-8)}{4L^2(\cos(M_2)-1)}\left(\frac{2\pi^2{A_1}^2-4{A_2}^2+8\pi^2{A_3}^2}{L}\right)\\
&+\frac{A_2Ebh_{\mathrm{mid}}^4t(8\cos(M_2)+3{M_2}^2+{M_2}^2\cos(M_2)-8)}{4L^2(\cos(M_2)-1)}\left(\frac{{A_2}^2{M_2}^2(\cos(M_2)+3)}{2L(\cos(M_2)-1)}\right)\\
&-\frac{A_2Ebh_{\mathrm{mid}}^4t(8\cos(M_2)+3{M_2}^2+{M_2}^2\cos(M_2)-8)}{4L^2(\cos(M_2)-1)}\left(\frac{2{B_1}^2\pi^2}{L}-\frac{2{b_1}^2\pi^2}{L}\right)=0, \qquad (3.24)
\end{aligned}
$$

$$
\begin{aligned}
\frac{\mathrm{dPE}}{\mathrm{d}A_3}&=\frac{4Ebh_{\mathrm{mid}}^2t^3\pi^4(8A_3-8a_3+C_1b_1)}{3L^3}\\
&+\frac{4A_3Ebh_{\mathrm{mid}}^4t\pi^2}{L^2}\left(\frac{2\pi^2{A_1}^2-4{A_2}^2+8\pi^2{A_3}^2}{L}-\frac{{A_2}^2{M_2}^2(\cos(M_2)+3)}{2L(\cos(M_2)-1)}\right)\\
&-\frac{4A_3Ebh_{\mathrm{mid}}^4t\pi^2}{L^2}\left(\frac{2\pi^2{a_1}^2-4{a_2}^2+8\pi^2{a_3}^2}{L}-\frac{{M_2}^2{a_2}^2(\cos(M_2)+3)}{2L(\cos(M_2)-1)}\right)\\
&+\frac{4A_3Ebh_{\mathrm{mid}}^4t\pi^2}{L^2}\left(\frac{2{B_1}^2\pi^2}{L}-\frac{2{b_1}^2\pi^2}{L}\right)=0, \qquad (3.25)
\end{aligned}
$$

$$
\begin{aligned}
\frac{\mathrm{dPE}}{\mathrm{d}B_1}&=\frac{2Eb^3h_{\mathrm{mid}}^2t\pi^4(B_1-b_1+C_1a_1-2C_1a_3)}{3L^3}+\frac{B_1Ebh_{\mathrm{mid}}^4t\pi^2}{L^2}\left(\frac{2{B_1}^2\pi^2}{L}-\frac{2{b_1}^2\pi^2}{L}\right)\\
&\times\frac{B_1Ebh_{\mathrm{mid}}^4t\pi^2}{L^2}\left(\frac{2\pi^2{A_1}^2-4{A_2}^2+8\pi^2{A_3}^2}{L}-\frac{{A_2}^2{M_2}^2(\cos(M_2)+3)}{2L(\cos(M_2)-1)}\right)\\
&-\frac{B_1Ebh_{\mathrm{mid}}^4t\pi^2}{L^2}\left(\frac{2\pi^2{a_1}^2-4{a_2}^2+8\pi^2{a_3}^2}{L}-\frac{{M_2}^2{a_2}^2(\cos(M_2)+3)}{2L(\cos(M_2)-1)}\right)=0 \qquad (3.26)
\end{aligned}
$$

and

$$
\begin{aligned}
\frac{\mathrm{dPE}}{\mathrm{d}C_1}&=2Fe+\frac{2C_1GJ\pi^2}{L}+\frac{Ebb_1h_{\mathrm{mid}}^2t^3\pi^4\,(8A_3-4A_1+4a_1-8a_3+7C_1b_1)}{6L^3}\\
&+\frac{Eb^3h_{\mathrm{mid}}^2t}{96L^3\sin(M_2/2)^2({M_2}^4-5\pi^2{M_2}^2+4\pi^4)}(6C_1{M_2}^8{a_2}^2-30C_1{M_2}^6{a_2}^2\pi^2)\\
&+\alpha(256B_1a_1\pi^8-512B_1a_3\pi^8-256a_1b_1\pi^8+512a_3b_1\pi^8+448C_1{a_1}^2\pi^8+6144C_1{a_3}^2\pi^8)\\
&-\alpha(560C_1{M_2}^2{a_1}^2\pi^6+112C_1{M_2}^4{a_1}^2\pi^4+24C_1{M_2}^4{a_2}^2\pi^4-7680C_1{M_2}^2{a_3}^2\pi^6)x\\
&-\alpha(1536C_1{M_2}^4{a_3}^2\pi^4-2048C_1a_1a_3\pi^8-320B_1{M_2}^2a_1\pi^6+64B_1{M_2}^4a_1\pi^4)\\
&+\alpha(640B_1{M_2}^2a_3\pi^6-128B_1{M_2}^4a_3\pi^4+320{M_2}^2a_1b_1\pi^6-64{M_2}^4a_1b_1\pi^4)\\
&-\alpha(640{M_2}^2a_3b_1\pi^6+128{M_2}^4a_3b_1\pi^4+2560C_1{M_2}^2a_1a_3\pi^6-512C_1{M_2}^4a_1a_3\pi^4), \qquad (3.27)
\end{aligned}
$$

where

$$
\alpha=\frac{Eb^3h_{\mathrm{mid}}^2t}{96L^3\sin(M_2/2)^2({M_2}^4-5\pi^2{M_2}^2+4\pi^4)}\sin(M_2/2)^2.
$$

The force–displacement curve for the numerical values of $E=2.1\,\mathrm{GPa}$, $\nu=0.3$, $a_1=0.5$, $b_1=0.5$, $h_{\mathrm{mid}}=5\,\mathrm{mm}$, $b=2\,\mathrm{mm}$, $t=0.2\,\mathrm{mm}$ and $L=100\,\mathrm{mm}$ is shown in figure 6*a*. The arch, when unconstrained, takes the deformation pathway OAT. This pathway corresponds to an asymmetric solution given in figure 6*b*. However, it can be observed in figure 6*a* that OAT cuts the axis $F=0$ only twice, indicating snap through but bistability. Incidentally, this case is similar to a planar fixed–fixed arch, where the asymmetric mode needs to be restricted for the arch to be bistable [9].

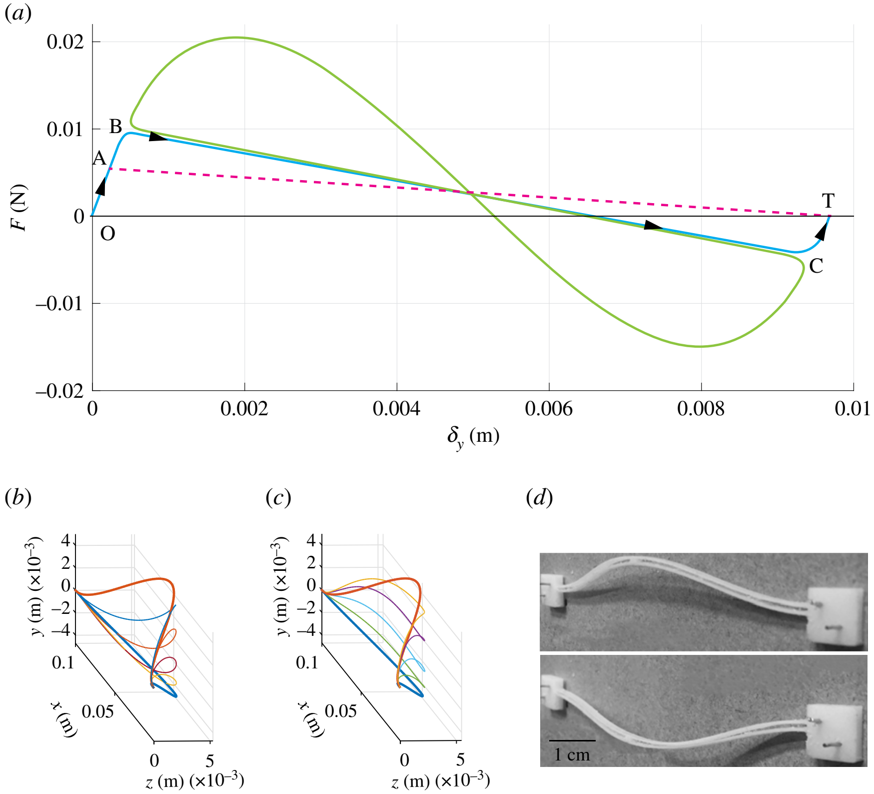

Figure 6. (*a*) Force–displacement characteristics and (*b* and *c*) deformations pathways of a fixed–fixed spatial arch with parameters: $a_1 = 0.5$, $b_1 = 0.5$, $h_{\text{mid}} = 5$ mm, $b = 2$ mm, $t = 0.2$ mm and $L = 100$ mm. (*d*) The two stable states of the arch in a 3D-printed prototype. (Online version in colour.)

Thus, by constraining the asymmetric mode of deformation in the arch, we facilitate the arch to take the path OABCT. In this deformation pathway, the arch switches symmetrically as shown in figure 6*c* and retraces the same curve during switching back. The constraining of asymmetric mode is physically achieved by connecting two arches at the mid-span as shown in the 3D-printed prototype in figure 6*d*.

4. Extensions using the spatial arch model

In this section, we illustrate that the spatial arch model described in the preceding section can be easily extended to: (i) spatial arches with as-fabricated shapes other than the fundamental profile, (ii) lateral-torsional buckling in planar arches and (iii) arches with eccentric loading.

(a) As-fabricated profiles other than the fundamental shapes

The equilibrium equations derived for spatial arches in §3a consider the first three modes in the as-fabricated shape. Let us consider a spatial arch with $a_1 = 0.5$, $a_3 = 0.2$, $b_1 = 0.5$, $h_{\text{mid}} = 5$ mm, $b = 2$ mm, $t = 0.5$ mm and $L = 100$ mm. Here, an additional third mode (a_3) is added to the starting shape of the hinged spatial arch considered previously. The force–displacement curve of the arch is shown in figure 7*a*. In comparison to figure 4*a*, we see that this arch can only switch symmetrically. The straight line shown in figure 7*a* corresponds to asymmetric mode of switching. However, the arch cannot deform in this mode of switching as the line cuts the curve corresponding to symmetric deformation only once. Thus, reaching any of the stable states becomes impossible once the arch starts deforming along this pathway. Furthermore, unlike the

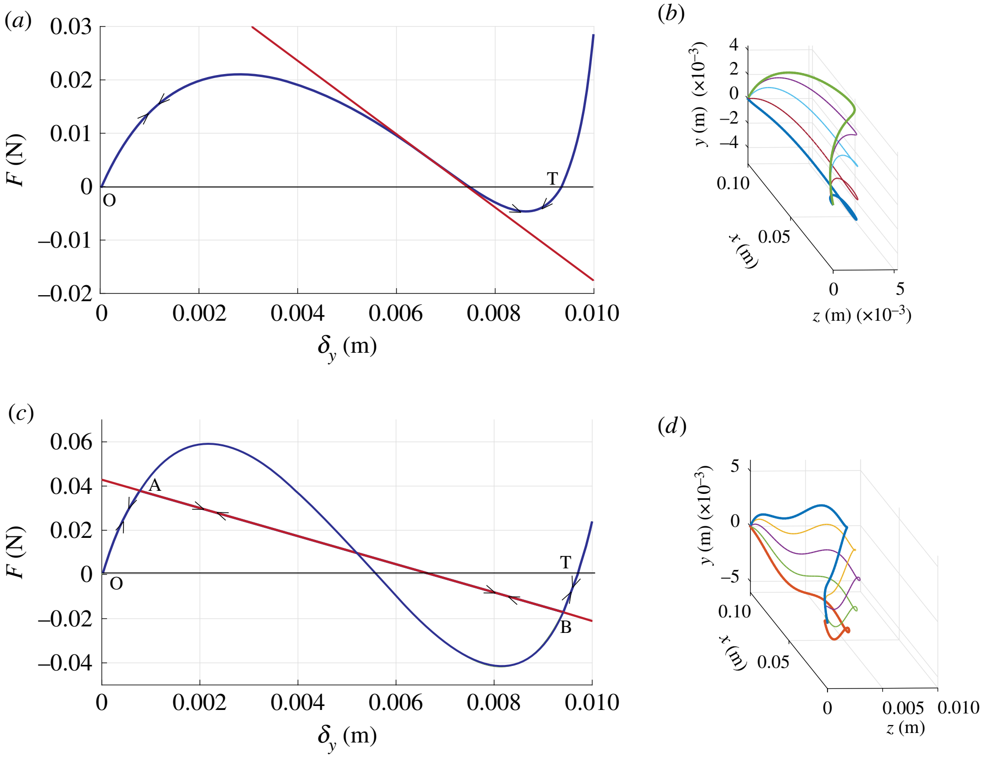

Figure 7. Force–displacement characteristics and deformation times-lapses of spatial arch with as-fabricated starting shapes with (*a* and *b*) $a_3 = 0.2$ (*a*,*b*) and (*c* and *d*) $a_7 = 0.1$ (*c*,*d*). (Online version in colour.)

previous examples, in this case, the asymmetric pathway is not reducing the force required for deforming. The arch-profiles in various stages of deformation between the stable states in the symmetric switching are depicted in figure 7*b*.

Arch-profiles with mode shapes other than the first three mode shapes can also be analysed using the model. However, we need to ensure that the all the mode shapes used for constructing the as-fabricated shape should be used in approximating the deformed profile as well. We noted in the three examples presented earlier that the arch can either switch symmetrically or asymmetrically. To capture these two pathways of switching, A_1 and A_2 are essential in approximating the deformed profile. We have to use the mode weights B_1 and C_1 for approximating $u(x)$ and $\phi(x)$. Since we can solve for five unknown mode weights, an additional mode weight can be added to $w(x)$, e.g. A_i. This enables us to use an additional a_i in the as-fabricated shape along with a_1 and a_2, and represent it as $w_0(x) = h_{\text{mid}}(a_1 w_1(x) + a_2 w_2(x) + a_i w_i(x))$. For example, the F-δ_y relations of a spatial arch with $a_1 = 0.5$, $a_7 = 0.1$, $b_1 = 0.5$, $h_{\text{mid}} = 5\,\text{mm}$, $b = 2\,\text{mm}$, $t = 0.5\,\text{mm}$ and $L = 100\,\text{mm}$ is given in figure 7*c*. The deformation pathway taken by the arch is OABT and the arch deforms as given in figure 7*d*.

(b) Lateral torsional buckling in planar arches

A planar arch is a special case of spatial arch with its curvature limited to a single plane. For instance, by taking all the b_is to be zero, the as-fabricated shape reduces to the xy plane. When the out-of-plane bending stiffness of the planar arch is comparable to the in-plane bending stiffness of the arch, the arch may deform out-of-plane and undergo lateral-torsional buckling. The compression energy formed in a planar arch when it deforms out of the plane is smaller than its in-plane deformation. This causes a reduction of the minimum force required to switch the bistable arch. We consider such an example next.

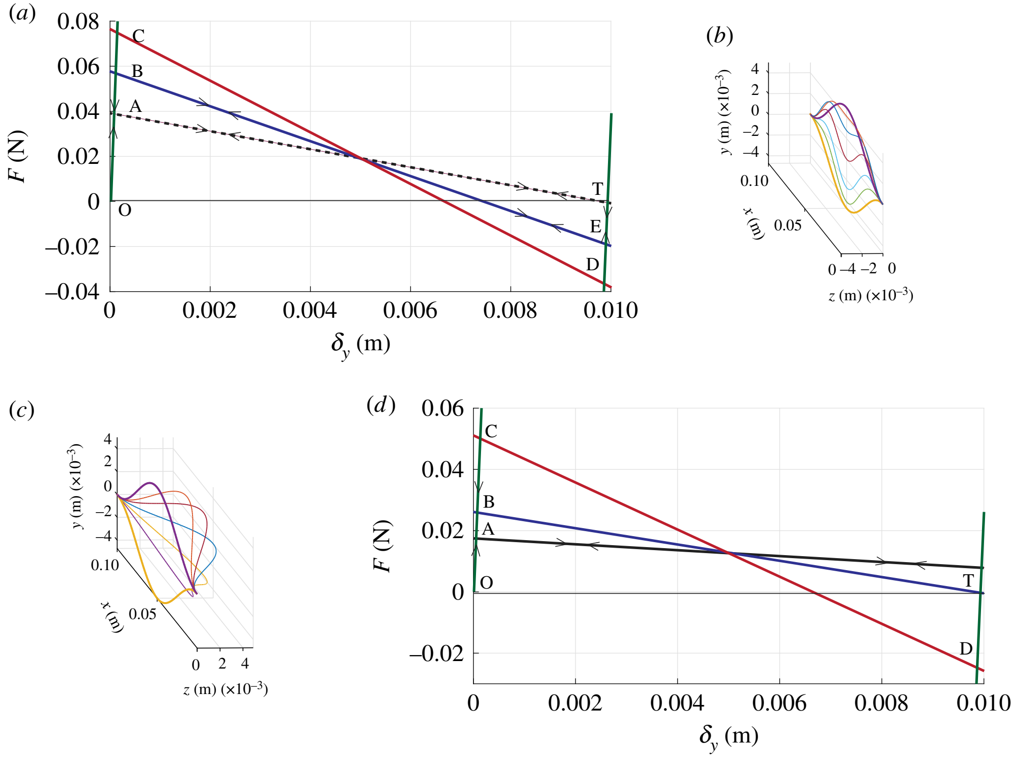

Figure 8. (*a*) Force–displacement characteristics and time-lapse of deformation of a planar arch with $a_1 = 1$, $b_1 = 0$, $h_{\mathrm{mid}} = 5$ mm, $b = 0.9$ mm, $t = 0.5$ mm and $L = 100$ mm, which shows bistability in the presence of a spatial deformation pathway. (*d*) Force–displacement characteristics and time-lapse of deformation of a planar arch with $a_1 = 1$, $b_1 = 0$, $h_{\mathrm{mid}} = 5$ mm, $b = 0.6$ mm, $t = 0.5$ mm and $L = 100$ mm, which is not bistable due to the presence of a spatial deformation pathway. (Online version in colour.)

The force–displacement characteristics for a planar arch with $a_1 = 1$, $h_{\mathrm{mid}} = 5\,\mathrm{mm}$, $b = 0.9\,\mathrm{mm}$, $t = 0.5\,\mathrm{mm}$, $L = 100\,\mathrm{mm}$, and with fixed–fixed boundary conditions are given in figure 8*a*. The path OAT represents the in-plane asymmetric switching that needs to be restricted so that the arch can attain the other stable state. When an arch is constrained to not take the asymmetric deformation pathway, it is expected to follow in-plane switching shown in figure 8*a* and indicated by the pathway OCDT. However, due to the presence of the lateral-torsional deformation, i.e. spatial deformation pathway (figure 8*c*), the arch prefers the force–displacement profile given by OBET. Thus, the arch switches with reduced switching force as indicated in figure 8*a*. The in-plane deformation corresponding to OBET is shown in figure 8*b*. Note that ignoring the spatial deformation in this problem leads to about 30% error in the prediction of actual critical force.

A contrasting case arises when the switching force reduces in such a way that it affects bistability of the arch. Figure 8*d* shows a force–displacement curve where the out-of-plane deformation path, AE, makes the arch not bistable. Note that if this arch with $a_1 = 0.5$, $b_1 = 0$, $h_{\mathrm{mid}} = 5\,\mathrm{mm}$, $b = 0.6\,\mathrm{mm}$, $t = 0.5\,\mathrm{mm}$ and $L = 100\,\mathrm{mm}$ were to be analysed as a planar arch, it would have shown bistability with force–displacement pathway OCDT. These observations are applicable to planar arches with pinned–pinned boundary conditions as well.

(c) Eccentrically loaded

When the arch is loaded eccentric to the xy plane at a distance e, it experiences a force as well as a moment. The moment causes the cross sections to rotate more compared to the case of the arch with only a point load. In the case of planar arch, the moment favours the lateral-torsional

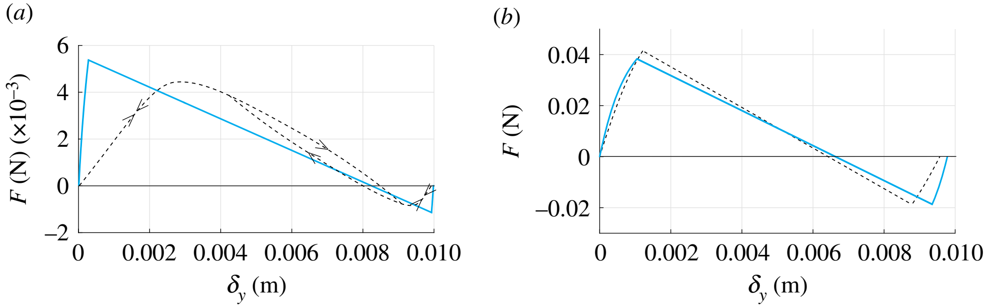

Figure 9. Comparison of force–displacement characteristics with (dashed curve) and without (solid curve) eccentric loading for spatial and planar pinned arches. (*a*) The planar arch parameters are $h_{mid} = 5$ mm, $b = 0.4$ mm, $t = 0.5$ mm, $L = 100$ mm, $E = 2.1$ GPa, $\nu = 0.3$, and $e = 10$ mm. (*b*) The spatial arch parameters are $a_1 = 1$, $b_1 = 0.5$, $h_{mid} = 5$ mm, $b = 2$ mm, $t = 0.5$ mm, $L = 100$ mm, $E = 2.1$ GPa, $\nu = 0.3$, and $e = 10$ mm. (Online version in colour.)

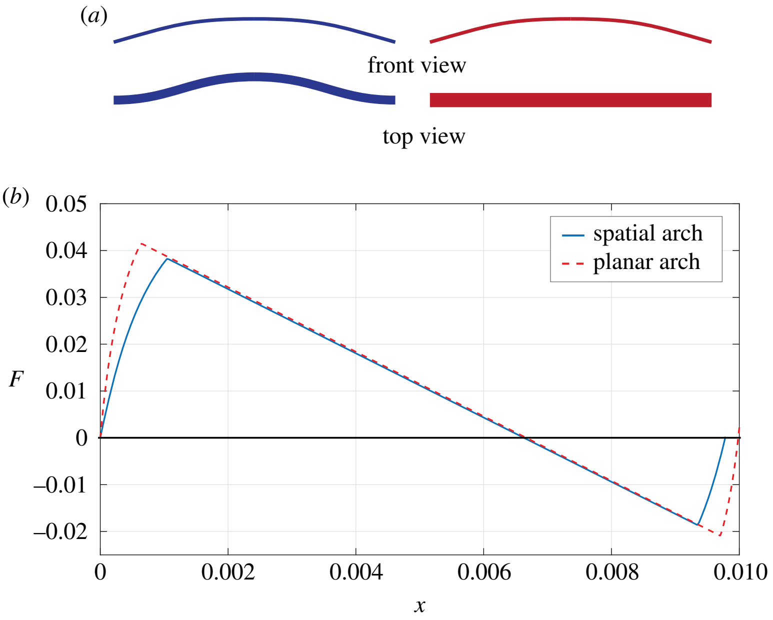

Figure 10. (*a*) Spatial and planar arches with same volume and pinned–pinned boundary conditions and (*b*) comparison of their force–displacement characteristics. (Online version in colour.)

mode of deformation. Figure 9*a* shows a comparison of planar pinned sine-curved arch with and without eccentric loading. The dashed curve corresponds to the case with eccentric loading with $e = 10$ mm for an arch with $h_{\mathrm{mid}} = 5$ mm, $b = 0.4$ mm, $t = 0.5$ mm, $L = 100$ mm, $E = 2.1$ GPa, and $\nu = 0.3$. We observe that eccentric loading reduces the switching and switch-back forces. The F-δ_y characteristic plot shown in figure 9*b* is of a spatial arch with $a_1 = 1$, $b_1 = 0.5$, $h_{\mathrm{mid}} = 5$ mm, $b = 2$ mm, $t = 0.5$ mm, $L = 100$ mm, $E = 2.1$ GPa, $\nu = 0.3$ and $e = 10$ mm. Here, the switching force increases due to the additional torsional energy in the cross sections due to the moment arising from eccentricity. This effect is not seen in figure 9*a* because of the smaller width considered there. It can be observed that the third point, where the force is zero, is not the same for both the loading cases in figure 9*b*. This is because of the rotation of cross sections of the arch. Due to the rotation, points attached eccentric to the arch move vertically. In this case, the spatial arch in its second stable has a positive rotation causing the point of application of load to go up. Hence, the dashed force–displacement curve shows a smaller travel of the mid-point of the arch between the two stable states.

5. A note

The result from the optimization problem that lead us to study spatial deformation pathways suggested that, for a given volume, a spatial distribution of material reduces the switching forces than the optimal in-plane solutions. Figure 10 shows a comparison between the pinned spatial arch considered in §3c to a planar pinned–pinned arch of the same volume. The reduction in forces can be accounted to reduced axial compression in the spatial arch and the reduced travel is due to the residue torsional energy in the spatial arch. The result from the model validate that the spatial deformation pathways reduce the switching forces in a bistable arch. This is relevant in two scenarios: while designing arches of reduced switching forces and while designing planar arches that should not deform out of plane.

6. Summary

In this paper, we discussed the analysis of doubly curved spatial arches that are bistable. The highlights of the paper are as follows:

- An analytical model that captures the coupling between in-plane and out-of-plane bending, and the torsion with an extension of St. Venant and Michell relationship that was given for arches with spatial deformation pathways.
- Analysis on spatial arches with varying as-fabricated shapes and boundary conditions for mid-point and eccentric loading.
- Analysis on spatial deformation pathways in planar arches, which is a special case of initial profile of spatial arches.
- Illustrative examples observing that the spatial deformation pathways reduce the switching forces bistable arches. In particular, it was shown that this reduction in switching forces in planar arches can also sometimes cause the arch to lose its bistability.

The desirable features of bistable structures such as two force-free stable states, negative structural stiffness, change in shape in the two stable states, snap-through action, and nonlinear force–displacement characteristic, find a wide range of applications. A few examples include switch-based applications such as micro-switches [17] and micro-relays [18], biomedical devices like easy-chairs for elderly [19] and deployable meta-implants [20], energy harvesters [21] and morphing structures [22,23]. Furthermore, spatial bistable arches will enrich the list of applications wherein the force needed to switch between the stable states ought to be minimal.

Authors' contributions. G.K.A. and S.P. designed the research, and S.P. developed the analytical model. Both the authors contributed to the writing of the manuscript and gave final approval for publication.

Competing interests. We declare we have no competing interests.

Funding. Financial support for this work was received from the Department of Science and Technology (DST), India under the Technology Initiative for the Disabled and the Elderly (TIDE) programme.

Acknowledgements. We thank DST, India for the financial support. We also thank Mr Suyog Mahulkar and Prof. Arakeri for their help with high-speed photography.

Appendix A

The bending strain energy, axial compression energy, torsional energy and work potential are obtained by substituting equations (3.6)–(3.10) in equations (2.11), (2.13), (2.17) and (2.19), respectively.

$$
\begin{aligned}
\mathrm{SE}_b &= \frac{EI_z}{2}\int_0^L \left(\frac{\mathrm{d}^2 w_0}{\mathrm{d}x^2} - \frac{\mathrm{d}^2 w}{\mathrm{d}x^2} + \phi\frac{\mathrm{d}^2 u_0}{\mathrm{d}x^2}\right)^2 \mathrm{d}x + \frac{EI_y}{2}\int_0^L \left(\frac{\mathrm{d}^2 u_0}{\mathrm{d}x^2} - \frac{\mathrm{d}^2 u}{\mathrm{d}x^2} - \phi\frac{\mathrm{d}^2 w_0}{\mathrm{d}x^2}\right)^2 \mathrm{d}x \\
&= \frac{Ebh_{\mathrm{mid}}^2 t^3}{24L^3}\pi^3 \left(\frac{\pi {A_1}^2}{2} - \frac{64A_1C_1b_1}{5} - 1\pi A_1 a_1 + 8\pi {A_2}^2 - 16\pi A_2 a_2 + \frac{81\pi {A_3}^2}{2}\right)
\end{aligned}
$$

$$\begin{aligned}
&+\frac{Ebh_{\mathrm{mid}}^2t^3}{24L^3}\left(\frac{3264A_3C_1b_1}{35}-81\pi A_3a_3+14\pi {C_1}^2{b_1}^2+\frac{64C_1a_1b_1}{5}-\frac{3264C_1a_3b_1}{35}\right)\\
&+\frac{Ebh_{\mathrm{mid}}^2t^3}{24L^3}\left(\frac{\pi {a_1}^2}{2}+8\pi {a_2}^2+\frac{81\pi {a_3}^2}{2}\right)-\frac{Eb^3h_{\mathrm{mid}}^2t\pi^3}{24L^3}\left(\frac{45\pi {C_1}^2a_1a_3}{4}+10\pi {C_1}^2{a_2}^2\right)\\
&\times\frac{Eb^3h_{\mathrm{mid}}^2t\pi^3}{24L^3}\left(8\pi {B_1}^2+\frac{64B_1C_1a_1}{5}-\frac{3264B_1C_1a_3}{35}-16\pi B_1b_1+\frac{5\pi {C_1}^2{a_1}^2}{4}\right)\\
&+\frac{Eb^3h_{\mathrm{mid}}^2t\pi^3}{24L^3}\left(\frac{243\pi {C_1}^2{a_3}^2}{4}-\frac{64C_1a_1b_1}{5}+\frac{3264C_1a_3b_1}{35}+8\pi {b_1}^2\right)
\end{aligned}\qquad\text{(A 1)}$$

$$\begin{aligned}
s&=\int_0^L\left[1+\frac{1}{2}\left(\frac{\mathrm{d}w}{\mathrm{d}x}\right)^2+\frac{1}{2}\left(\frac{\mathrm{d}u}{\mathrm{d}x}\right)^2\right]\mathrm{d}x\\
&=L+\frac{{B_1}^2h_{\mathrm{mid}}^2\pi^2}{L}+\frac{h_{\mathrm{mid}}^2\pi^2({A_1}^2+4{A_2}^2+9{A_3}^2)}{4L}
\end{aligned}\qquad\text{(A 2)}$$

$$\begin{aligned}
s_{\mathrm{initial}}&=\int_0^L\left[1+\frac{1}{2}\left(\frac{\mathrm{d}w_0}{\mathrm{d}x}\right)^2+\frac{1}{2}\left(\frac{\mathrm{d}u_o}{\mathrm{d}x}\right)^2\right]\mathrm{d}x\\
&=L+\frac{{b_1}^2h_{\mathrm{mid}}^2\pi^2}{L}+\frac{h_{\mathrm{mid}}^2\pi^2({a_1}^2+4{a_2}^2+9{a_3}^2)}{4L}
\end{aligned}\qquad\text{(A 3)}$$

$$\begin{aligned}
\mathrm{SE_c}&=\frac{1}{2}p(s_{\mathrm{initial}}-s)\\
&=\frac{Ebh_{\mathrm{mid}}^4t\pi^4({A_1}^2+4{A_2}^2+9{A_3}^2+4{B_1}^2-{a_1}^2-4{a_2}^2-9{a_3}^2-4{b_1}^2)^2}{32L^3}
\end{aligned}\qquad\text{(A 4)}$$

$$\begin{aligned}
\mathrm{SE}_t&=\frac{GJ}{2}\int_0^L\left(\frac{\mathrm{d}\phi}{\mathrm{d}x}\right)^2\mathrm{d}x\\
&=\frac{{C_1}^2GJ\pi^2}{L}
\end{aligned}\qquad\text{(A 5)}$$

$$\begin{aligned}
\delta_y&=w_0\left(\frac{1}{2}\right)-w\left(\frac{1}{2}\right)-e\phi\left(\frac{L}{2}\right)\\
&=-2C_1e-h_{\mathrm{mid}}(A_1-A_3)+h_{\mathrm{mid}}(a_1-a_3)
\end{aligned}\qquad\text{(A 6)}$$

$$\begin{aligned}
\mathrm{WP}&=-F\delta_y\\
&=-F(-2C_1e-h_{\mathrm{mid}}(A_1-A_3)+h_{\mathrm{mid}}(a_1-a_3))
\end{aligned}\qquad\text{(A 7)}$$

Appendix B

The force–displacement characteristics obtained from the analytical modelling show good agreement with FEA. A comparison of illustrative examples discussed in this work with FEA is given in figure 11. The solid curves represent results from analytical model and dashed curves are obtained from FEA done in ABAQUS. In ABAQUS, continuum tetrahedral elements are used with quasi-static dynamic-implicit analysis for all four cases. In figure 11*a*, asymmetric and symmetric deformation pathways of a spatial arch with hinged and fixed support discussed in §3a (figure 4) are compared. In obtaining the analytical solution, five mode shapes are used. The asymmetric and asymmetric deformations, wherein the magnitude of force ranges from 0.04 N to −0.03 N, have mean errors of 0.0012 N and 0.0015 N, respectively. The analytical approach solves this problem withing a CPU time of 187 s compared to 14 151 s of FEA and thus, it is 70 times faster than FEA. However, this speed varies from problem to problem. Nonetheless, analytical method always solve the problem much faster than FEA.

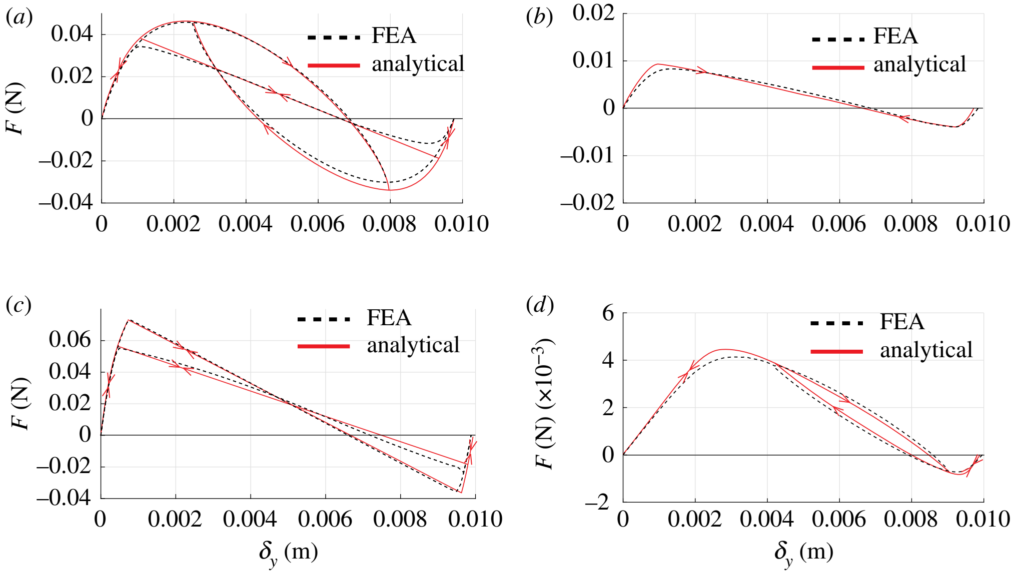

Figure 11. Comparison of force–displacement characteristics obtained from analytical modelling with FEA in ABAQUS for (*a*) pinned–pinned spatial, (*b*) fixed–fixed spatial arch, (*c*) fixed–fixed planar arch with spatial deformation and (*d*) pinned–pinned arch with an eccentric load. (Online version in colour.)

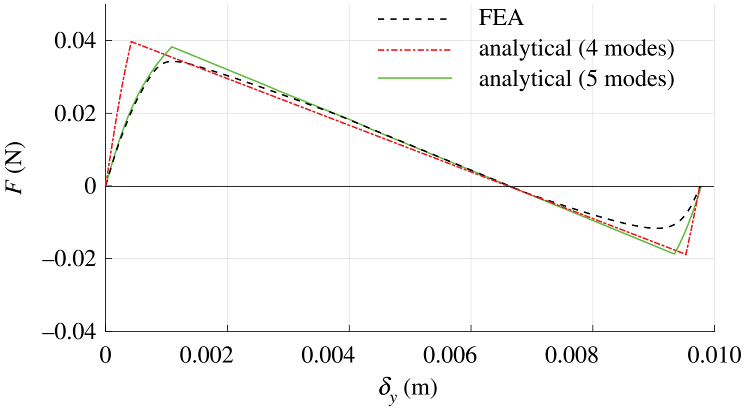

Figure 12. Comparison of force–displacement characteristics obtained from analytical modelling with FEA in Abaqus for varying number of mode shapes. (Online version in colour.)

Note that the error from the numerical solution is larger at the points where the arch switches from one deformation pathway to the other. By using a larger number of mode shapes for approximating the deformed profiles, this error can be minimized as shown in figure 12. With five mode shapes, the force–curve shows closer agreement compared to the one with four mode shapes.

The cases of fixed–fixed spatial arch (figure 6), fixed–fixed planar arch with spatial deformations (figure 8), and pinned–pinned spatial arch with eccentric loading (figure 9*a*) are shown in figure 11*b*–*d*, respectively. The geometric and material parameters considered are the same as the ones in their respective examples considered in §§3 and 4.

References

1. Timoshenko SP. 1936 *Theory of elastic stability, by S. Timoshenko....* New York, NY: McGraw-Hill Book Company, Incorporated.
2. Vlasov VZ. 1959 Thin-walled elastic beams. *PST Catalogue* **428**.
3. Pi YL, Bradford M, Tong GS. 2010 Elastic lateral–torsional buckling of circular arches subjected to a central concentrated load. *Int. J. Mech. Sci.* **52**, 847–862. (doi:10.1016/j.ijmecsci.2010.02.003)
4. Papangelis JP, Trahair NS. 1987 Flexural-torsional buckling of arches. University of Sydney.
5. Mohri F, Azrar L, Potier-Ferry M. 2002 Lateral post-buckling analysis of thin-walled open section beams. *Thin-Wall. Struct.* **40**, 1013–1036. (doi:10.1016/S0263-8231(02)00043-5)
6. Simitses GJ, Hutchinson J. 1976 *An introduction to the elastic stability of structures*. Malabar, FL: Kreiger Publishing Company.
7. Vangbo M. 1998 An analytical analysis of a compressed bistable buckled beam. *Sens. Actuators A Phys.* **69**, 212–216. (doi:10.1016/S0924-4247(98)00097-1)
8. Fung Y, Kaplan A. 1952 Buckling of low arches or curved beams of small curvature. NACA Technical Note 2840.
9. Qiu J, Lang JH, Slocum AH. 2004 A curved-beam bistable mechanism. *J. Microelectromech. Syst.* **13**, 137–146. (doi:10.1109/JMEMS.2004.825308)
10. Palathingal S, Ananthasuresh G. 2017 Design of bistable arches by determining critical points in the force-displacement characteristic. *Mech. Mach. Theory* **117**, 175–188. (doi:10.1016/j.mechmachtheory.2017.07.009)
11. Guest S, Pellegrino S. 2006 Analytical models for bistable cylindrical shells. *Proc. R. Soc. A* **462**, 839–854. (doi:10.1098/rspa.2005.1598)
12. Sobota P, Seffen KA. 2017 Effects of boundary conditions on bistable behaviour in axisymmetrical shallow shells. *Proc. R. Soc. A* **473**, 20170230. (doi:10.1098/rspa.2017.0230)
13. Love AEH. 2013 *A treatise on the mathematical theory of elasticity*. Cambridge, UK: Cambridge University Press.
14. Ojalvo M, Demuts E, Tokarz F. 1969 Out-of-plane buckling of curved members. *J. Struct. Div.* **95**, 2305–2318.
15. Palathingal S, Ananthasuresh G. 2018 A bilateral relationship between stable profiles of pinned–pinned bistable shallow arches. *Int. J. Solids Struct.* **143**, 183–193. (doi:10.1016/j.ijsolstr.2018.03.006)
16. ABAQUS C. 2015 Analysis user manual, Version 2016.
17. Yadav D, Murthy NS, Palathingal S, Shekhar S, Giridhar M, Ananthasuresh G. 2019 A two-terminal bistable electrothermally actuated microswitch. *J. Microelectromech. Syst.* **28**, 540–549. (doi:10.1109/JMEMS.84)
18. Qui J, Lang JH, Slocum AH, Strumpler R. 2003 A high-current electrothermal bistable MEMS relay. In *Proc. - MEMS 2003, IEEE the Sixteenth Annual Int. Conf. on Micro Electro Mechanical Systems, Kyoto, Japan, 19–23 January*, pp. 64–67. Piscataway, NJ: IEEE.
19. Sarojini D, Lassche T, Herder J, Ananthasuresh G. 2016 Statically balanced compliant two-port bistable mechanism. *Mech. Mach. Theory* **102**, 1–13. (doi:10.1016/j.mechmachtheory.2016.03.016)
20. Bobbert F, Janbaz S, Zadpoor A. 2018 Towards deployable meta-implants. *J. Mater. Chem. B* **6**, 3449–3455. (doi:10.1039/C8TB00576A)
21. Pellegrini SP, Tolou N, Schenk M, Herder JL. 2013 Bistable vibration energy harvesters: a review. *J. Intell. Mater. Syst. Struct.* **24**, 1303–1312. (doi:10.1177/1045389X12444940)
22. Emam SA, Inman DJ. 2015 A review on bistable composite laminates for morphing and energy harvesting. *Appl. Mech. Rev.* **67**, 060803. (doi:10.1115/1.4032037)
23. Hu N, Burgueño R. 2015 Buckling-induced smart applications: recent advances and trends. *Smart Mater. Struct.* **24**, 063001. (doi:10.1088/0964-1726/24/6/063001)